Adaptive Beamforming for Wireless Powering of a Network of Ultrasonic Implants

Max L. Wang*, Ajay Singhvi*, Gift Nyikayaramba*, Boris Murmann, and Amin Arbabian
Department of Electrical Engineering, Stanford University, Stanford, CA, USA

***Abstract*—Networks of implantable medical devices (IMDs) capable of operating deep in the body are crucial for many novel diagnostic and therapeutic applications. Ultrasound (US) power and data transfer has shown promise for minimally invasive, deeply implantable devices wherein an external portable base station is used to power, coordinate, and communicate with IMD networks. Efficient US power transfer requires focused radiation on the IMD receiver, but current US arrays may have unwanted side lobes due to large transducer pitch with focusing being especially challenging when the application requires simultaneous powering of only a subset of IMDs while avoiding other IMDs in the network. In this work, we devise an adaptive beamforming approach, implemented using a least mean squares (LMS) algorithm, that allows for precise control over both the peak and null regions in the transmitted US beam. We demonstrate successful beamforming with multiple peaks at desired angles and transmit frequencies. In conjunction, we also show significant nulling (>40 dB) in regions where implants should not be activated.**

***Index Terms*—adaptive beamforming, implant, LMS, ultrasound, wireless power transfer**

I. Introduction

Wireless implantable medical devices (IMDs) have become valuable tools for monitoring, diagnosing, and treating many different medical conditions. Aggressive miniaturization of IMDs down to millimeter dimensions without sacrificing functionality has been made possible by innovations in electronics, packaging, and in-body wireless power transfer and communication. This has led to devices that can be more easily implanted where they are needed and enabled a range of applications including gut sensing, drug delivery, and neuromodulation [1]–[3]. Miniaturization of IMDs also opens up the possibility of forming networks of implants which can be placed anywhere in the body, enabling closed-loop therapies requiring coordination between sensing, processing, and stimulation as shown in Fig. 1 [3].

Ultrasound (US) has been proposed for powering and communicating with minimally invasive, deeply implanted IMDs [4]. The relatively low propagation loss and short acoustic wavelengths enables efficient coupling to miniaturized implants and focusing down to millimeter-sized spots at large depths. An ultrasonic power transfer system typically includes a power transmitter which sends US power through the body to

This work was supported by the NIH under award numbers R01EB025867 and R21AI163489, the NSF CAREER Award under award number ECCS-1454107, and the Dr. Robert Noyce and Rambus Corporation Stanford Graduate Fellowships.

* M. L. Wang, A. Singhvi, and G. Nyikayaramba contributed equally to this work.

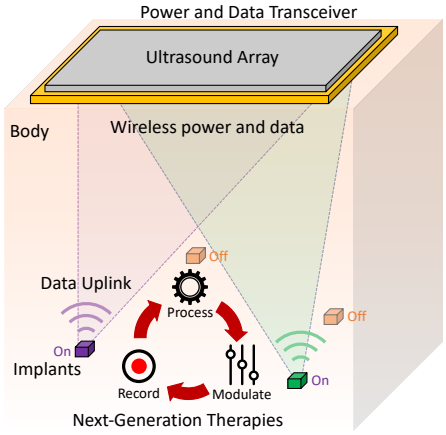

Fig. 1. Conceptual diagram of an IMD network enabling next-generation therapies.

piezoelectric receivers which convert the acoustic waves into electrical signals for the implants. While maximizing power transfer efficiency requires focusing power to the implant, most previous demonstrations of US powering, both in tissue phantom or *in vivo*, use unfocused US power transmitters or know the implant receiver location *a priori* to maintain a robust link. For example, in [1] a US-powered implantable gut biosensor was tested across multiple days. Since the location of the implant was only approximately known, a single-element unfocused US transducer was used to ensure reliable power-up *in vivo* at the expense of efficiency. Thus, there is a tradeoff between efficiency and tolerance to misalignment, making it challenging to reliably achieve high efficiency *in vivo*.

To break this tradeoff, US phased arrays have been used to electronically focus the energy on the implants [4]–[6]. Nonetheless, determining the optimal phasing of the power transmitter elements is needed to ensure precise alignment of the focus to the implant. In [5], signals from the implant were used to compute the implant location which was then used to determine the beamforming delays. Benedict et al. [6] improved the focusing by using time reversal beamforming which does not degrade with tissue inhomogeneity or scattering. While these works improved power transfer, they provide little control over side lobe and null regions, which may lead to worse overall efficiency as well as undesired or unpredictable implant activation.

In this work, we follow an approach based on one described by Widrow et al. [7], in which they demonstrated the

2022 IEEE International Ultrasonics Symposium (IUS) | 978-1-6654-6657-8/22/$31.00 ©2022 IEEE | DOI: 10.1109/IUS54386.2022.9958008

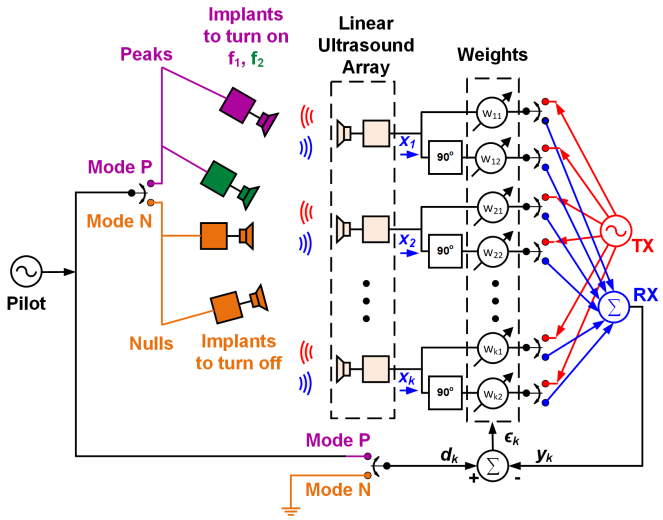

Fig. 2. Block diagram showing the structure of the implemented adaptive US beamformer.

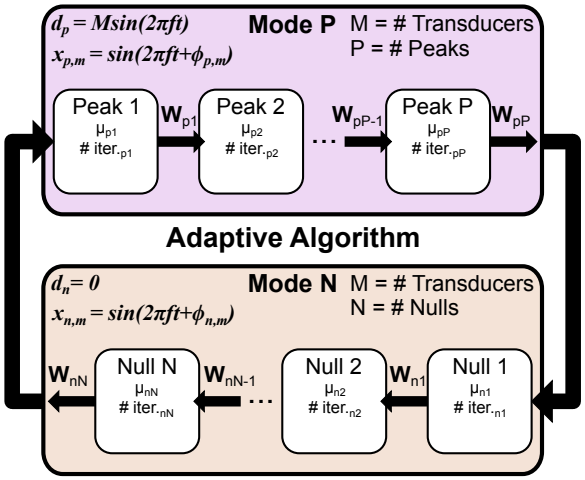

Fig. 3. Flow-chart illustrating the adaptive beamforming training procedure which iterates over each desired peak and null.

successful adaptation of an antenna array to simultaneously form main lobes in desired look directions and nulls in the directions of undesired interferers. We explore the utility of a similar adaptive beamforming scheme for wireless US powering across a wide range of peak and null configurations, multiple US array parameters, and a variety of US frequencies — focusing on the tradeoffs involved as well as the system-level implications of implementing such a scheme.

II. Implementation

A. Adaptive Beamforming

As can be seen in Fig. 1, efficiently powering networks of IMDs in the body requires providing focused US power to each device either simultaneously or sequentially. Additionally, we might want to power only a subset of the implants in the network requiring us to generate US beam patterns with complete programmability of not just the peak locations but also direct control over the null regions.

Conventional transmit beamforming [8], [9] allows us to form nulls and peaks using a fixed set of weights and delays. However, they don't allow for the controlled formation of different patterns as required by the multi-functional closed-loop IMD network. Furthermore, they would be limited in their ability to respond to the introduction of additional sources of noise and interference in the system. Thus, in order to have the desired programmability we instead turn to adaptive beamforming approaches which dynamically tune beamforming parameters to maximize or minimize the power sent to a particular location.

B. Training Setup and Process

The adaptive US beamformer implemented in this work is shown in Fig. 2. It consists of a linear array of K ultrasonic transducers spaced $\frac{\lambda_0}{2}$ apart, with an operating frequency, f_0, of 1 MHz. During training, the signal, x_k, from each array element is split into two components that are 90° out of phase. Each of these signals is then multiplied by a corresponding weight, w_{ij}, and summed to form the overall output, y_k, before being compared to the desired signal, d_k. The resulting error signal, ε_k, is then input into the adaptive processor which adjusts the weights using the least mean squares (LMS) algorithm [7] to form the optimal, desired beam pattern.

As an initialization step, we propose sweeping a US beam over the region of interest to identify the implants and determine the required access patterns. Once initialized, a two-mode pilot signal based adaptation process is carried out by using the desired peaks/nulls to provide an initial weighting for the array elements to start selective power transfer, with the pilot signal chosen to have spectral and temporal characteristics that are similar to those of the transmitted US power signal. To adapt the beamforming over time to account for potential misalignments from breathing or sudden movements, training could continue in the background using the uplink signals from the implants during typical operation. Note that while the primary function of the US transducer array is to act as a transmitter to power on the implants, it functions as a receiver throughout the adaptation process. Once adaptation is completed, the obtained weights are fed to the transducer elements in order to produce the desired beam pattern.

A flow chart illustrating the adaptation process is shown in Fig. 3. In Mode P, each of the implants residing at the locations we want to activate (peak) sends out a pilot signal in a sequential manner. For each implant, this pilot signal also serves as the desired signal at the adaptive processor. The LMS algorithm is used to create a peak at the current implant. This process is repeated until peaks are formed at all the target implants after which the system switches to Mode N.

In Mode N, implants residing at locations we do not want to activate (null) sequentially send out pilot signals. The desired signal just becomes the zero signal. In a manner similar to Mode P, the LMS algorithm is run to create the nulls one-by-one at the desired locations with Mode N ending once the last null is formed. To ensure that the weights settle to their steady state values for a given combination of peaks and nulls,

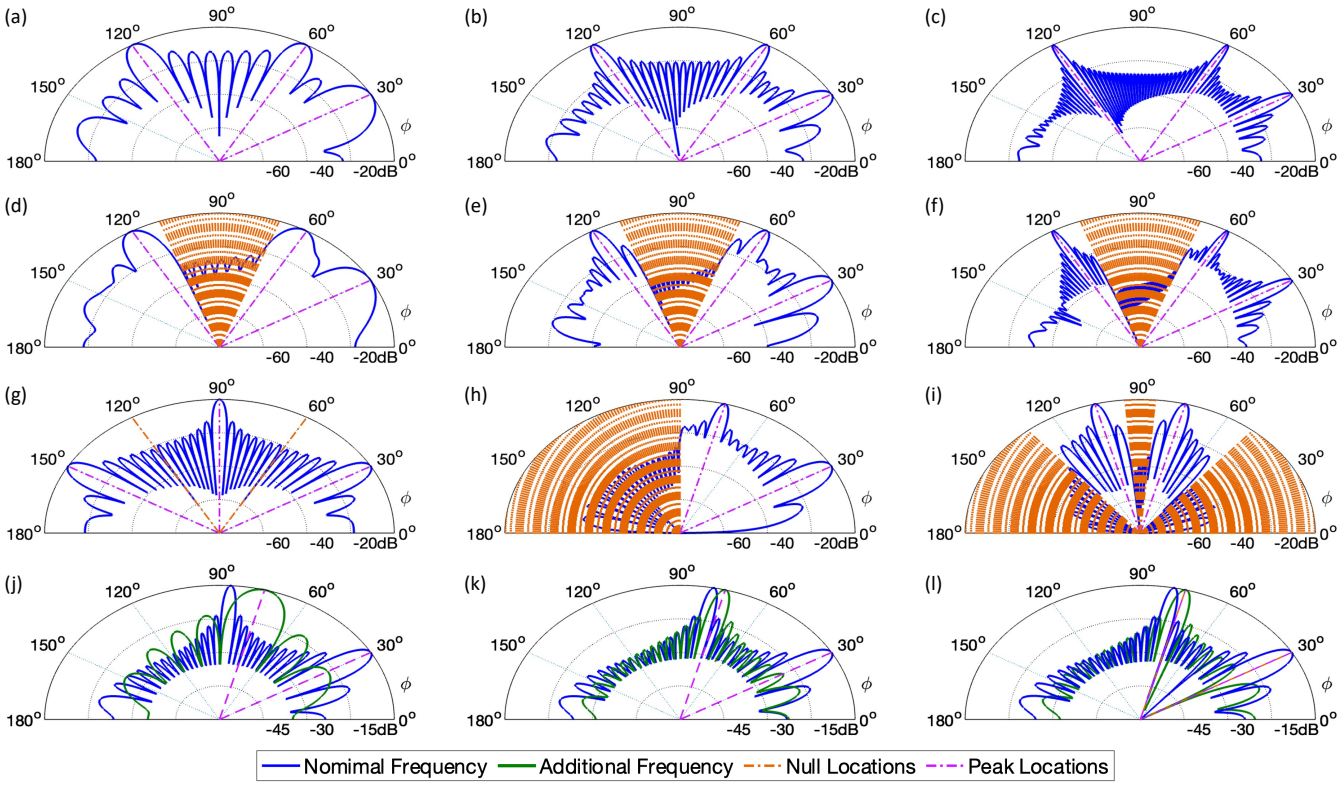

Fig. 4. Far-field US beam patterns for: (a)-(c) 16, 32, and 64 element US array configurations with the same peak locations (30°, 60°, 120°) and no null locations specified; (d)-(f) 16, 32, and 64 element US array configurations with the same peak locations (30°, 60°, 120°) and explicit null regions (70° to 110°) specified; (g)-(i) 32 element single-frequency US array with different peak and null locations (j) 32 element multi-frequency US array peaks specified at 1 MHz (nominal frequency) and 0.25 MHz (additional frequency) (k) 32 element multi-frequency US array peaks specified at 1 MHz (nominal frequency) and 0.75 MHz (additional frequency) (l) 32 element multi-frequency US array with the peak at 1 MHz explicitly nulled at 0.75 MHz and vice-versa.

several Mode P-to-Mode N sequences are run before the final set of values is extracted.

In addition to the spatial selectivity of the adaptive beamformer, we also investigated its frequency selectivity. To do this, the pilot signals were made to vary in frequency at the various peaks and nulls, with a similar adaptation process carried out as described above.

C. Simulation Transducer Parameters and Setup

We carried out both electrical and acoustic simulations to verify our proposed adaptive beamforming scheme. Electrical simulations included creating directivity plots using far-field approximations [10]. Three-dimensional US simulations were performed in MATLAB with the Field II toolbox to verify the results from the adaptation and directivity plots [11]. Linear arrays were constructed with each element having 500 μm width and $\lambda_0/2$ (770 μm) pitch. The length of the elements was set such that the overall aperture would be square. Each element is divided into 20 sub-elements for the simulation. Note that the coordinate system is laid out such that the array sits in the xy-plane. The spatial resolution of the simulation was set to be 1 mm^2 to provide sufficient accuracy while maintaining reasonable simulation time.

III. Results

A. Directivity Simulations

Utilizing the training setup, process, and simulation parameters described in Section II, we first show results of US transmit beamforming via the far-field directivity plots seen in Fig. 4. The directivity plots are created for a variety of adaptation parameters in terms of the peak and null locations (discrete or contiguous regions), operating US frequency, and the size of the US array.

Fig. 4(a)-(c) show that as we scale up the number of array elements $(16, 32, 64)$, we have tighter control over the beamwidths, reduced side-lobe strength, and the potential for more closely spaced nulls or peaks. However, this comes at the expense of additional hardware for both the US electronics as well as the adaptive processor. Fig. 4(d)-(f) show beam patterns generated by utilizing the same US array configurations and peak locations as in Fig. 4(a)-(c) respectively, but with an explicitly specified null region from 70° to 110° — demonstrating much lower side-lobe strength than when nulls were not explicitly provided to the adaptive beamformer. Fig. 4(g)-(i) show beam patterns generated for a 32-element US array with different peak and null locations specified, with the power of the side-lobes in the null locations being significantly lower than that of the main-lobes in the peak locations. These

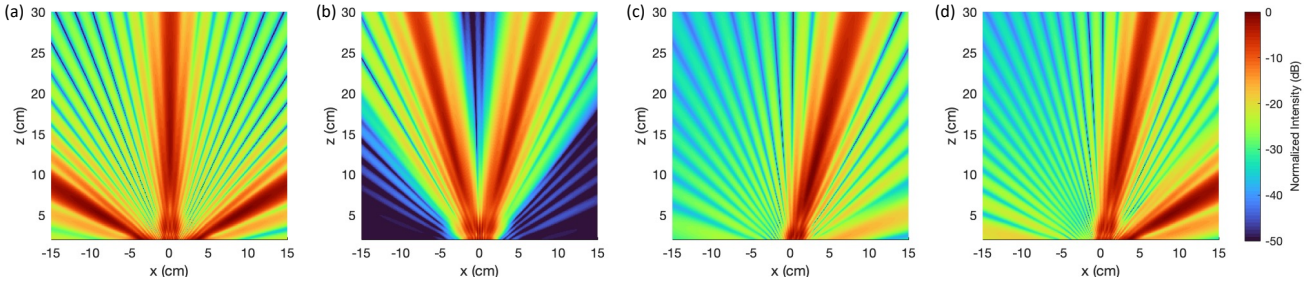

Fig. 5. Simulated ultrasonic beam patterns: 32 element single-frequency pattern with (a) 3 peak and 2 null locations (b) 2 peak locations and 3 null regions; 32 element multi-frequency pattern with one peak at (c) 0.75 MHz and another at (d) 1 MHz.

results show how our proposed adaptive beamformer can be utilized to improve robustness by only powering up a specific subset of implants in a network of IMDs.

Finally, Fig. 4(j)-(l) include directivity plots corresponding to two different US frequencies. We show that in addition to being able to specify the locations of multiple peaks and nulls, we can also specify the frequency. This could be useful when designing IMD networks as we can resonate implants at different frequencies, allowing us to individually control them even if they are co-located. However, the peak/null locations and frequency are not completely independent degrees of freedom. Fig. 4(j),(k) show that even though only one peak is specified at each frequency, the directivity plot shows two peaks. The unwanted peak is from the peak specified at the other frequency, though it is shifted because of the frequency difference. The shift increases with the difference in frequency as can be seen in Fig. 4(j),(k). In Fig. 4(l), we show an interesting case where the peak at one frequency is explicitly nulled at another frequency.

To ensure that the adaption process was robust to noise, we carried out additional simulations by adding a zero-mean Gaussian noise source to each weight in the system, while maintaining an SNR of 10 dB. The resulting beam patterns largely resembled those in Fig. 4. Averaging was also shown to further improve performance in the presence of noise.

B. Field II Simulations

We then conduct end-to-end US simulations in Field II [11] to verify the results from the far-field directivity plots shown in Fig. 4. The US array was laid out to sit in the xy-plane, with the beamforming plots in Fig. 5 showing intensity in the xz-plane at y = 0 cm. Fig. 5(a),(b) correspond to the 32 element, single-frequency configurations used in Fig. 4(g),(i) respectively. The US simulations show good agreement with the far-field directivity plots, verifying that the analysis is accurate. Note that the peak transmit intensity occurs at the focal plane of the array, which is 10 cm for the 32-element array. Fig. 5(c),(d) correspond to the additional frequency (0.75 MHz) and the nominal frequency (1 MHz) respectively for the configuration shown in Fig. 4(l) — demonstrating that the US simulations once again match the far-field directivity plots.

IV. Conclusion

In this work, adaptive beamforming techniques were applied to optimize the wireless delivery of power from a linear ultrasound array to a network of implants. The goal was to steer an ultrasonic beam to a subset of implants that require activation (peak locations) while simultaneously minimizing the power delivered to implants that need to stay off (null locations). To achieve this goal, a pilot signal approach was employed to create the desired peaks and nulls using the LMS algorithm to adjust the weights in the adaptive signal processor. We investigated various peak-null patterns, the effect of varying array and LMS algorithm parameters, as well as the frequency selectivity of the array with results showing that the proposed approach provides both robustness and flexibility. Future work will include experimental demonstrations along with investigation of second order effects like propagation losses, multi-path propagation.

References

[1] S. Baltsavias *et al.*, "In vivo wireless sensors for gut microbiome redox monitoring," *IEEE Transactions on Biomedical Engineering*, vol. 67, no. 7, pp. 1821–1830, 2019.

[2] M. L. Wang *et al.*, "A wireless implantable potentiostat for programmable electrochemical drug delivery," in *2021 IEEE Biomedical Circuits and Systems Conference (BioCAS)*. IEEE, 2021, pp. 1–4.

[3] F. Laiwalla *et al.*, "A distributed wireless network of implantable sub-mm cortical microstimulators for brain-computer interfaces," in *2019 41st Annual International Conference of the IEEE Engineering in Medicine and Biology Society (EMBC)*. IEEE, 2019, pp. 6876–6879.

[4] M. L. Wang *et al.*, "Closed-loop ultrasonic power and communication with multiple miniaturized active implantable medical devices," in *2017 IEEE International Ultrasonics Symposium (IUS)*. IEEE, 2017, pp. 1–4.

[5] M. L. Wang, T. C. Chang, and A. Arbabian, "Ultrasonic implant localization for wireless power transfer: Active uplink and harmonic backscatter," in *2019 IEEE International Ultrasonics Symposium (IUS)*. IEEE, 2019, pp. 818–821.

[6] B. C. Benedict *et al.*, "Time reversal beamforming for powering ultrasonic implants," in *2021 10th International IEEE/EMBS Conference on Neural Engineering (NER)*. IEEE, 2021, pp. 647–650.

[7] B. Widrow *et al.*, "Adaptive antenna systems," 1967.

[8] T. Costa *et al.*, "An integrated 2d ultrasound phased array transmitter in cmos with pixel pitch-matched beamforming," *IEEE Transactions on Biomedical Circuits and Systems*, vol. 15, no. 4, pp. 731–742, 2021.

[9] P. Tipsawat *et al.*, "32 element piezoelectric micromachined ultrasound transducer (pmut) phased array for neuromodulation," *IEEE Open Journal of Ultrasonics, Ferroelectrics, and Frequency Control*, pp. 1–1, 2022.

[10] S. Orfanidis, *Electromagnetic Waves and Antennas*, 2016.

[11] J. A. Jensen, "Field: A program for simulating ultrasound systems," in *10th Nordic-Baltic Conference on Biomedical Imaging, vol. 4, supplement 1, part 1: 351–353*, 1996.